Journal of Applied Fluid Mechanics, Vol. 18, No. 11, pp. 2697-2710, 2025.
Available online at www.jafmonline.net, ISSN 1735-3572, EISSN 1735-3645.
https://doi.org/10.47176/jafm.18.11.3425

Direct Numerical Simulation of Turbulent Channel Flow with Spanwise System Rotation and Velocity Slip on Suction Wall

A. Moosaie[1,2†], Zh. Najafi-Kashkooli[1] and H. I. Andersson[3]

[1] *Department of Mechanical Engineering, Yasouj University, Yasouj 75918-74934, Iran*
[2] *Department of Mechanical Engineering, Isfahan University of Technology, Isfahan 84156-83111, Iran*
[3] *Department of Energy and Process Engineering, Norwegian University of Science and Technology, Trondheim, Norway*

†*Corresponding Author Email: moosaie@iut.ac.ir*

ABSTRACT

Direct numerical simulations are conducted to investigate the turbulent flow of an incompressible Newtonian fluid in a channel at a fully-developed state. The channel rotates steadily around its spanwise axis. A hydrophobic coating on the suction side introduces the velocity slip, while the pressure side maintains a no-slip boundary condition. Flow statistics are reported for different slip intensities, considering both rotating and stationary channel cases. Two main sources of asymmetry relative to the channel centerline are identified: slip at the suction wall and rotational effects. Results show that a linear region forms in the mean velocity profile of the rotating channel with slip, similar to the no-slip case, and this linear region widens as the rotation number increases. Distributions of velocity fluctuation RMS values and Reynolds shear stress are presented and analyzed for various conditions. Additionally, the structure of near-wall streaks and the evolution of instantaneous streamwise vorticity are examined.

Article History

Received February 5, 2025
Revised June 3, 2025
Accepted June 17, 2025
Available online September 3, 2025

Keywords:

Direct numerical simulation
Turbulent channel flow
Spanwise system rotation
Hydrophobic suction wall
Slip condition
Mean flow asymmetry

1. INTRODUCTION

The advancement of micro- and nano-technology allowed the manufacturing of hydrophobic surfaces which led to macroscopic flow slip on the walls. This leads to a significant reduction in viscous drag across both laminar and turbulent flow regimes. The use of such technology has great potential applications in ship manufacturing, submarine industries, etc. Besides drag reduction applications, it is also desirable to develop hydrophobic or hydrophilic non-toxic coatings on ships and submarines to prevent fouling on the wetted surfaces (Youngblood et al., 2003). Furthermore, investigating the influence of wall slip boundary conditions on the dynamics of turbulent wall-bounded flows is fundamentally important.

In the past, extensive research has focused on investigating non-rotating turbulent channel flows using direct numerical simulations (DNS) with no-slip wall condition. There are much less publications on DNS of turbulent channel flow either with system rotation or with slip condition. But, the combined effect of these two has not been yet addressed. In the present work, using the DNS technique, we present the statistics of a fully-developed spanwise-rotating turbulent channel flow, in which a slippery wall is assumed on the suction side whereas the no-slip condition is imposed on the pressure wall. Although this constitutes a problem of generic fundamental interest, this study might as well pertain to viscous drag reduction applications in rotating systems such as turbomachines as well as geophysical and astrophysical applications. Cooling of rotating systems, such as radars, by fluid flow could also be a potential area of application, where the conduits are drag-reduced by hydrophobic coating to decrease the required pumping power of fluid circulation system.

Experimental investigations have confirmed that flows over hydrophobic surfaces can be described by the Navier-Stokes equations supplemented with slip boundary condition (Watanabe et al., 1999; Tretheway & Meinhart, 2002; Choi et al., 2003; Ou et al., 2004). In the area of numerical simulations, Min and Kim (2004) conducted a DNS study of turbulent channel flow at $\mathrm{Re}_\tau = 180$ with Re_τ being the shear Reynolds number, employing slip (hydrophobic) walls and applying Navier's slip formula. Min and Kim (2004) demonstrated that introducing slip only in the streamwise direction leads to drag reduction and a weakening of near-wall coherent structures, notably streamwise vortices. Conversely, allowing slip in the spanwise direction as well diminishes the drag-reducing effect and may even result in drag increase. Later, Min and Kim (2005) extended their work by performing DNS to examine how slip boundary conditions influence the

laminar-to-turbulence transition. Their results indicated that streamwise slip tends to delay the onset of turbulence, leading to an increase in the critical Reynolds number, while spanwise slip promotes earlier transition, thereby lowering the critical Reynolds number. Martin and Boyd (2006) carried out numerical simulations of fluid flow and heat transfer within a laminar boundary layer, applying Navier's slip boundary condition. In the thermal analysis, two temperature boundary conditions were examined: one imposing a temperature jump at the slip wall, and the other enforcing continuity of temperature. Unlike the classical Blasius (1908) solution for no-slip walls, the slip flow exhibited a non-self-similar 2D velocity field rather than the well-known self-similar profile. Later, Martin and Boyd (2010) extended their investigation to a wedge flow using Falkner-Skan equations, solving the problem numerically with a marching method under Navier's slip model. They observed that the presence of slip reduced both skin friction and the thickness of the boundary-layer, and they also addressed the corresponding heat transfer characteristics. In a separate study, Busse and Sandham (2012) explored the influence of an anisotropic slip-length boundary condition on turbulent channel flows using DNS. By conducting simulations at two different Reynolds numbers, they also assessed how Reynolds number variations impact the flow behavior.

Several studies have also examined how turbulence is influenced in the proximity of walls with super-hydrophobic coating. Martell et al. (2009) investigated turbulent channel flows with inhomogeneous wall conditions, modeling ridge and post geometries to represent adjacent air-pocket interfaces. Afterwards, additional DNS studies exploring the modulation of laminar and turbulent flows in the vicinity of superhydrophobic surfaces were presented by Martell et al. (2010) and Park et al. (2013).

Moosaie and Panahi-Kalus (2021) conducted direct numerical simulations (DNS) of turbulent flow and passive scalar transport like temperature in a channel, applying velocity slip and temperature jump conditions at one of the walls. More recently, Moosaie and Sharifian (2024) carried out a numerical study of steady laminar flow around a circular cylinder subjected to a velocity slip boundary condition. They used an analytical solution provided by Atefi (1991), see also Moosaie (2022), to validate their solution. Moosaie (2024) provided an exact analytical solution for conjugate heat transfer and thermoelastic behavior of a hollow spherical particle immersed in a low Reynolds number slip flow in the framework of Stokesian dynamics. Also, Moosaie (2025) provided approximate analytical solutions for heat convection from a sphere with temperature jump condition at low Peclet numbers using Oseen's theory.

A turbulent channel flow rotating about its spanwise axis has been investigated by a number of authors, both experimentally and numerically. Johnston et al. (1972) have experimentally studied this problem and found that the profiles of the mean streamwise velocity become asymmetric with respect to the channel centerline in the rotating flow. This effect was attributed to the stabilizing Coriolis effect on the suction side and its destabilizing Coriolis effect on the pressure side. More recent measurements have been conducted by Nakabayashi and Kitoh (1996, 2005) using hot-wire anemometry and by Visscher and Andersson (2011) and Visscher et al. (2011) using particle-image velocimetry (PIV). Some experimental data have been also reported by Maciel et al. (2003). These experimental data have confirmed the previous experimental and DNS findings and provided more insights into the turbulence mechanics and structures. Numerical simulations of spanwise rotating channel flow have been presented by a number of authors. Speziale and Thangam (1983) have simulated a laminar incompressible flow in a spanwise-rotating channel with rectangular cross-section. They have found that by increasing the speed of rotation, the velocity profiles become asymmetric and the maximum velocity tends towards the suction wall. Launder et al. (1987) and, Launder and Tselepidakis (1994) have studied this problem using the Reynolds-averaged Navier-Stokes (RANS) approach with the use of a second-moment closure model. This problem has been also investigated by employing DNS. Kristoffersen and Andersson (1993) have performed the first DNS study and found out that the maximum mean velocity moves towards the suction wall. Also, for low to intermediate rotation rates, the peaks of turbulence intensities decrease near the suction wall while they increase in the vicinity of the pressure wall, as compared to the non-rotating channel. Bech and Andersson (1997) have conducted the DNS of rotating Couette flow under strong system rotation and deduced that the system rotation results in a considerable weakening of turbulence structures. Grundestam et al. (2008) carried out DNS of channel flow subjected to spanwise rotation, varying the rotation number to investigate how the system's angular velocity influences turbulent structures. Narasimhamurthy and Andersson (2015) have studied a spanwise-rotating ribbed channel flow in order to scrutinize the simultaneous effect of channel rotation and wall roughness on turbulence. They have used the same DNS code, called MGLET, as employed in the present study. Jagadeesan et al. (2022) performed a DNS of turbulent rib-roughened channel flow rotating about its spanwise axis using MGLET.

The literature survey, presented above, shows that the simultaneous effect of spanwise system rotation and wall slip condition in turbulent flows has not been yet addressed. Thus, we focus on this problem here and present for the first time the first- and second-order turbulence statistics of this flow configuration at a nominal friction Reynolds number $\mathrm{Re}_\tau = 194$. Also, the turbulence production due to mean flow shear and system rotation is studied. In this paper, the case of slip condition on the suction wall is addressed.

This paper is structured in the following way: Section 2 outlines the governing equations. In Section 3, the numerical methods are described, along with the validation process for incorporating the wall slip condition into the code. Section 4 provides an overview of the simulation details, while Section 5 focuses on the presentation and discussion of the results. The concluding remarks are provided in Section 6.

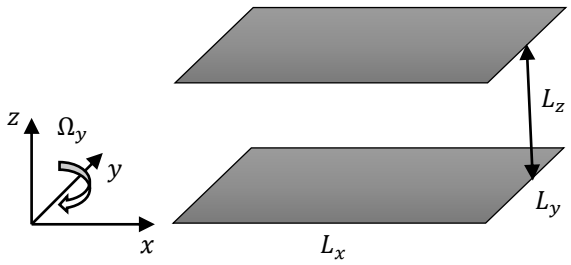

Fig. 1 Channel geometry and the coordinate system.

2. GOVERNING EQUATIONS

A turbulent channel flow rotating about its spanwise axis is directly simulated here. The flow is assumed to be incompressible and the fluid viscous stress is Newtonian. The thermal effects are disregarded and the flow is assumed to be isothermal. The channel configuration and the coordinate system are depicted in Fig. 1. The whole system is rotating about the spanwise axis y with a constant negative angular velocity Ω. Thus, the Coriolis term is to be taken into account in Navier-Stokes equations as a source term. Thus, the flow governing equations are the following continuity and Navier-Stokes equations:

$$\frac{\partial U_i}{\partial x_i} = 0, \tag{1}$$

$$\frac{\partial U_i}{\partial t} + U_j \frac{\partial U_i}{\partial x_j} = -\frac{1}{\rho}\frac{\partial P}{\partial x_i} + \nu \frac{\partial^2 U_i}{\partial x_j \partial x_j} - 2\varepsilon_{ijk}\Omega_j U_k, \tag{2}$$

in which ρ, ν, P, U_i, ε_{ijk} and Ω_j are density, kinematic viscosity, pressure, velocity, Levi-Civita permutation symbol and the constant angular velocity of the whole system, respectively. The Einstein's index summation convention holds throughout this paper. The rotation about the spanwise direction y is considered here. So, only $\Omega_2 = \Omega_y = \Omega$ is non-zero and the other two components vanish, i.e. $\Omega_1 = \Omega_3 = 0$.

The no-slip wall condition is assumed on the channel pressure wall at $z = 2h$. The slip wall condition is imposed on the channel suction wall at $z = 0$, that is, the wall shear stress is proportional to the wall slip velocity. This boundary condition is written on the suction wall for both wall shear stresses τ_{zx} and τ_{zy} in x and y directions, respectively:

$$\tau_{zx}(z=0) = \mu \left.\frac{\partial U}{\partial z}\right|_{z=0} = \lambda\, U(z=0), \tag{3}$$

$$\tau_{zy}(z=0) = \mu \left.\frac{\partial V}{\partial z}\right|_{z=0} = \lambda\, V(z=0), \tag{4}$$

where μ is the dynamic viscosity of the fluid. Also, $\lambda \geq 0$ is the slip coefficient [28] which is related to the slip length L_s via $L_s = \mu/\lambda$. In general, the slip coefficient λ, or alternatively the slip length L_s, depends on the shear rate (Choi et al., 2003), thermophysical properties of the fluid and the surface (Atefi, 1991), etc. We assume a constant λ in this report. Also, the slip coefficient λ in x and y directions are assumed to be the same. In general, however, they could be different. Non-dimensionalizing the above boundary conditions, we have

$$\left.\frac{\partial \tilde{U}}{\partial \tilde{z}}\right|_{\tilde{z}=0} = \mathrm{Tr}\, \tilde{U}(\tilde{z}=0), \tag{5}$$

$$\left.\frac{\partial \tilde{V}}{\partial \tilde{z}}\right|_{\tilde{z}=0} = \mathrm{Tr}\, \tilde{V}(\tilde{z}=0), \tag{6}$$

in which $\tilde{z} = z/h$ is the dimensionless wall distance, $\tilde{U} = U/U_{\mathrm{b,nos}}$ and $\tilde{V} = V/U_{\mathrm{b,nos}}$ are the dimensionless streamwise and spanwise velocities, respectively. Also, h and $U_{\mathrm{b,nos}}$ are the half of the channel width and the bulk streamwise velocity across the non-rotating no-slip channel, respectively. Trostel number is defined via $\mathrm{Tr} = h\lambda/\mu$. It quantifies the amount of wall slip (Atefi, 1991). Trostel number is connected to the slip length via $\mathrm{Tr} = h/L_s$. In this paper, we prefer the Trostel number instead of the slip length, as it is a dimensionless description for the amount of wall slip. Two limiting cases are notable; $\mathrm{Tr_b} = 0$ represents the full slip condition (zero wall shear stress) whereas $\mathrm{Tr_b} = \infty$ yields the no-slip condition, where $\mathrm{Tr_b}$ is the Trostel number at the suction wall.

3. NUMERICAL METHODS AND VALIDATION

The Navier-Stokes Eqs. (1) and (2) are solved by the MGLET code (Manhart, 2004). Equation (2) is discretized in space by a finite volume method with second-order formal accuracy on a Cartesian non-uniform grid according to the volume-balance method of Schumann (1975) and is integrated in time by a third-order Runge-Kutta scheme using the explicit low-storage formulation (Williamson, 1980). The incompressibility condition Eq. (1) is enforced by the projection method of Chorin (1968) and Temam (1969). The Poisson equation for pressure is iteratively solved by the strongly implicit procedure (SIP) (Stone, 1968). A staggered arrangement of flow quantities is used, i.e., momentum fluxes by velocity components are stored on cell faces whereas the pressure is stored at the cell centers.

A central finite difference scheme of second-order formal accuracy is used to enforce the slip boundary condition at the suction wall. Two wall-adjacent cells, one real cell and one ghost cell, are shown in Fig. 2 along with the mesh parameters. By using a central difference scheme for the velocity gradient and a central interpolation scheme

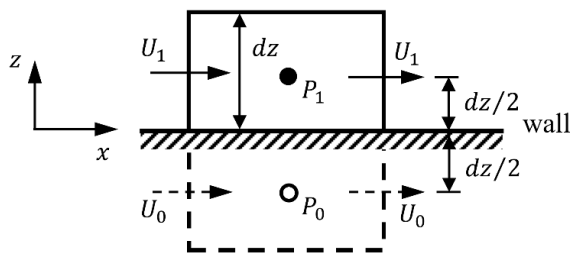

Fig. 2 Staggered computational cells at the wall for the enforcement of slip boundary condition

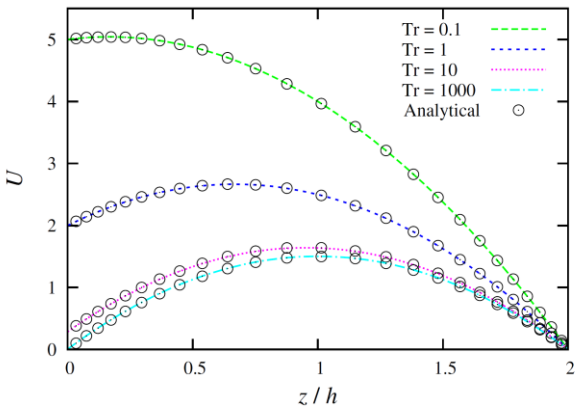

Fig. 3 Streamwise velocity profiles in laminar channel flow with slip boundary condition at the suction wall with different Trostel numbers

for the velocity, both at the wall, the following second-order formulae for the staggered velocities of the ghost cell in x and y directions are obtained in terms of the real cell velocities, grid spacing, channel half-width and $\mathrm{Tr_b}$:

$$U_0 = \frac{1-\beta}{1+\beta}U_1, \qquad V_0 = \frac{1-\beta}{1+\beta}V_1, \tag{7}$$

where $\beta = \mathrm{Tr_b}\ \mathrm{d}z/2h$.

In order to implement the system rotation to the MGLET code, we modified the subroutine that computes the right-hand side (RHS) of the Navier-Stokes equation. This subroutine is called by the Runge-Kutta time stepping subroutine. The rotation term $-2\varepsilon_{ijk}\Omega_j U_k$ in Eq. (2) is added to the RHS subroutine as a source term and is calculated once at every Runge-Kutta substep.

The MGLET code has been extensively validated and applied in various studies, particularly for DNS of both Newtonian and non-Newtonian turbulent channel flows, see e.g. Moosaie and Manhart (2011, 2013, 2015, 2016), Moosaie et al. (2015) and Moosaie (2016). Also, this code has been used by Narasimhamurthy and Andersson (2015) to directly simulate turbulent spanwise-rotating flow in a ribbed channel to study the simultaneous effect of wall roughness and spanwise system rotation on turbulence. In this work, we add the slip boundary condition to this code. Thus, only the slip condition is to be validated. For this purpose, two test cases are considered. The first one is a steady laminar Newtonian channel flow with slip at $z = 0$ and no-slip at $z = 2h$. The slip condition in MGLET is treated in an explicit manner. To evaluate the time accuracy of our implementation, we use an unsteady problem as the second validation example. That is the Stokes' second problem with slip condition.

3.1 Steady Validation Case: Laminar Channel Flow with Wall Slip

Navier-Stokes equations for this flow configuration can be analytically solved, and the following velocity distribution is obtained:

$$U(z) = \frac{1}{2}Az^2 + C_1 z + C_2, \tag{8}$$

in which $A = \frac{1}{\mu}\frac{\partial P}{\partial x}$ is a constant and the integration constants C_1 and C_2 are obtained by assuming slip condition (5) at $z = 0$ wall and no-slip condition at $z = 2h$ wall:

$$C_1 = -\frac{2Ah\mathrm{Tr_b}}{2\mathrm{Tr_b}+1}, \qquad C_2 = -\frac{2Ah^2}{2\mathrm{Tr_b}+1}. \tag{9}$$

Various laminar flow simulations for different values of $\mathrm{Tr_b}$ have been conducted using MGLET and the so-obtained velocity profiles are compared with the above analytical solution in Fig. 3. An excellent agreement is established which demonstrates that the slip boundary condition is correctly implemented in MGLET.

3.2 Unsteady Validation Case: Stokes' Second Problem with Wall Slip

The laminar flow in a half-plane induced by an oscillating wall is called the Stokes' second problem. The wall oscillates harmonically according to $U_0 \cos \omega t$. Thus, U_0 and ω are the wall oscillation amplitude and angular frequency, respectively. The Navier-Stokes equations for this problem reduce to

$$\frac{\partial U}{\partial t} = \nu \frac{\partial^2 U}{\partial z^2}, \tag{10}$$

which is subjected to the following initial and boundary conditions:

$$U(z,t{=}0) = BU_0 e^{-kz}\cos(kz+\phi), \tag{11a}$$

$$\mu \left.\frac{\partial U}{\partial z}\right|_{z=0} = \lambda[u(0,t) - U_0 \cos \omega t], \tag{11b}$$

$$U(\infty,t) = 0. \tag{11c}$$

In Eqs. (11a) and (11b), the parameters are given by $B = 1/\sqrt{2\gamma^2+2\gamma+1}$, $\phi = \tan^{-1}[\gamma/(1+\gamma)]$, $\gamma = k\mu/\lambda$ and $k = \sqrt{\omega/2\nu}$, respectively. The exact analytical solution to this problem is given by Wang et al. (2011) as

$$U(z,t) = BU_0 e^{-kz}\cos[\omega t - (kz+\phi)]. \tag{12}$$

This problem is as well solved by MGLET, taking a domain of $(L_x,L_y,L_z) = (5,0.1,5)$ discretized by $(N_x,N_y,N_z) = (500,2,5000)$ equidistant finite volumes. The parameters are set to $\nu = 0.001$, $\omega = 1.0$, $U_0 = 1.0$, $\gamma = 2.2361$ and $\delta t = 0.0001$. The velocity profiles at different dimensionless time instants ωt as a function of the dimensionless wall distance $z\sqrt{\omega/2\nu}$ are plotted in Fig. 4, along with the analytical solution (12). The agreement between the results demonstrates the accuracy of the slip condition implementation for time-dependent flows. In order to quantify the accuracy, the absolute error in predicting the wall velocity is plotted versus time in Fig. 5. The wall velocity is chosen as an error indicator because it is very sensitive to the accuracy of the numerical schemes. The absolute error is computed by taking the analytical value of the wall velocity, that is $u(0,t) = BU_0\cos[\omega t - \phi]$, as the reference value. It is seen that the absolute error always remains below $10^{-3}U_0$, for the chosen set of parameters.

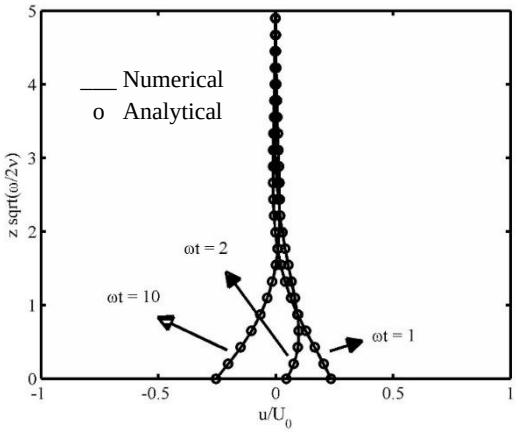

Fig. 4 Velocity profiles of Stokes' second problem at various dimensionless time instants ωt versus the dimensionless wall distance $z\sqrt{\omega/2\nu}$

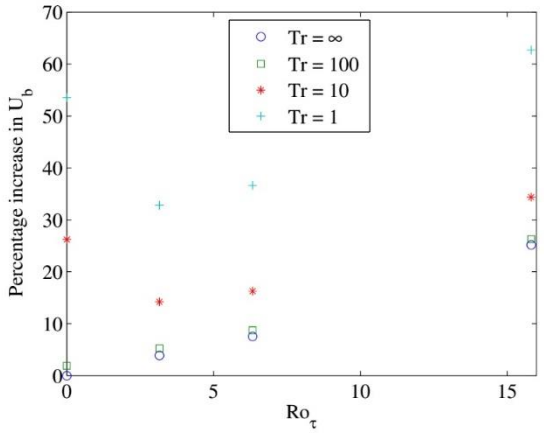

Fig. 5 Percentage increase in U_b compared to the non-rotating no-slip flow for different Trostel numbers as a function of the rotation number

4. SIMULATION SETUP

The flow domain is considered as a computational box with the dimensions of $(L_x,L_y,L_z) = (4\pi h,4\pi h/3,2h)$ in which x, y and z are the streamwise, spanwise and wall-normal directions, respectively. A Cartesian mesh with $(N_x,N_y,N_z) = (220,180,128)$ finite volumes is used to discretize the flow domain. This sums up to about 5 million computational cells. The computational mesh is uniform in the periodic x and y directions whereas it is non-uniform in the inhomogeneous z direction in order to capture the near-wall sharp gradients. The fluid viscosity and driving pressure gradient are chosen to result in $\mathrm{Re}_\tau = 194$ for the non-rotating case with the no-slip condition. The nominal friction Reynolds number is defined as

$$\mathrm{Re}_\tau = \frac{hu_{\tau*}}{\nu}, \qquad u_{\tau*}^2 = \left|\frac{1}{\rho}\frac{\partial P}{\partial x}\right|, \tag{13}$$

where $u_{\tau*}$ is the friction velocity of the non-rotating channel with no-slip condition and $\partial P/\partial x$ is the exerted average pressure gradient driving the flow. Based on $u_{\tau*}$, the distances and velocities can be normalized, e.g.

$$z^+ = \frac{zu_{\tau*}}{\nu}, \qquad U^+ = \frac{U}{u_{\tau*}}. \tag{14a}$$

The driving mean pressure gradient is kept constant for all simulations reported in this paper. This implies that the bulk velocity is not the same for different simulations. Thus, the results and conclusions presented in this paper shall be interpreted as for the case of a constant mean pressure gradient and not of a constant bulk velocity.

The normalized grid spacing reads

$$(\Delta x^+,\Delta y^+,\Delta z^+_{\min},\Delta z^+_{\max}) = (11.08,4.51,0.73,5.37) \tag{14b}$$

where $\Delta z^+_{\min}$ and $\Delta z^+_{\max}$ are the minimum grid resolution at the wall and the maximum grid resolution at the channel centerline, respectively. Also, the system angular velocity Ω is normalized in the following way to yield the friction rotation number Ro_τ:

$$\mathrm{Ro}_\tau = \frac{2\Omega h}{u_{\tau*}}. \tag{15}$$

The flows were simulated over a sufficiently long duration to ensure that each flow case reaches its fully-developed state. Then, flow statistics were collected over a long period of time, i.e. about 50 flow-through time units. The flow quantities were averaged in time and also in the homogeneous x and y directions in order to enhance the quality of the statistics.

5. RESULTS AND DISCUSSIONS

Statistical results of DNS (mean velocity profiles, Reynolds stresses and production terms) are presented and discussed here. Different sets of rotation and Trostel numbers are chosen, i.e. $\mathrm{Ro}_\tau = 0$, 3.16, 6.33 and 15.82, and $\mathrm{Tr}_\mathrm{b} = 1$, 10, 100 and ∞. The channel is rotated in such a way that the bottom wall at $z = 0$ becomes the suction side whereas the top wall at $z = 2h$ becomes the pressure side.

Sixteen different simulations with different rotation and Trostel numbers are conducted in this work, as listed in table 1 along with the percentage increase in the streamwise bulk velocity U_b. The change in U_b is calculated using the bulk velocity of the non-rotating channel flow with the no-slip condition as the reference value. The observed trends are as follows. At a constant rotation number, U_b increases by decreasing Trostel number (increasing slip). At a constant Trostel number, the behavior is somewhat more complicated. For small amounts of slip, i.e. for $\mathrm{Tr}_\mathrm{b} = \infty$ and 100, U_b increases by increasing the rotation number. However, for high levels of slip, specifically when $\mathrm{Tr}_\mathrm{b} = 10$ and 1, U_b initially decreases and then increases as the rotation number rises. This behavior of U_b versus Ro_τ is shown in Fig. 5.

5.1 Mean Velocity Profiles

The first-order statistics of mean velocity profiles for flows with different rotation and Trostel numbers are

Table 1 Rotation and Trostel numbers of presented simulations along with the percentage increase in the bulk velocity compared to the non-rotating flow with no-slip condition

Simulation #	Rotation number Ro_τ	Trostel number Tr_b	Percentage increase in U_b
1	0.0	1	53.57%
2	0.0	10	26.23%
3	0.0	100	1.87%
4	0.0	∞	0.0%
5	3.16	1	32.82%
6	3.16	10	14.21%
7	3.16	100	5.26%
8	3.16	∞	3.89%
9	6.33	1	36.63%
10	6.33	10	16.26%
11	6.33	100	8.73%
12	6.33	∞	7.56%
13	15.82	1	62.72%
14	15.82	10	34.36%
15	15.82	100	26.29%
16	15.82	∞	25.2%

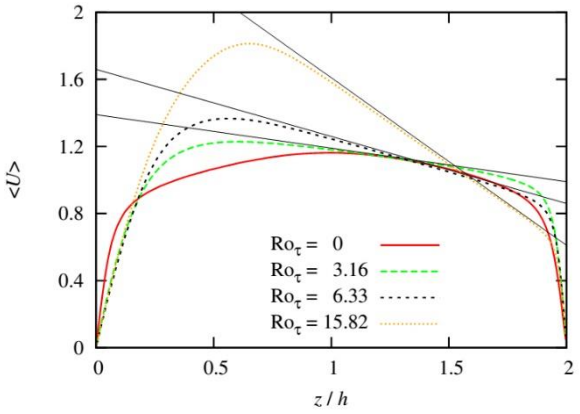

Fig. 6 Mean velocity profiles for different Rotation numbers with $Tr_b = \infty$. Thin, black, solid lines represent straight lines with slope 2Ω

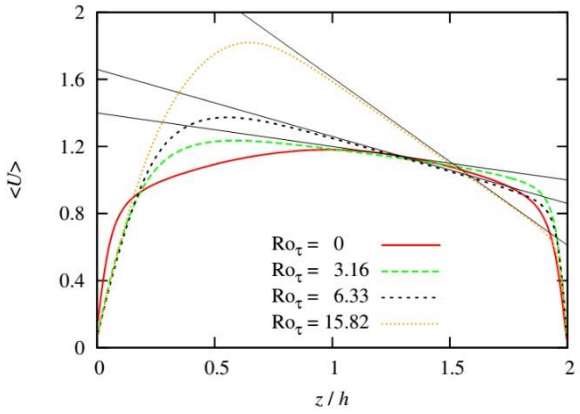

Fig. 7 Mean velocity profiles at different Rotation numbers with $Tr_b = 100$. Thin, black, solid lines represent straight lines with slope 2Ω

presented and discussed here. Figure 6 shows the profiles of the mean streamwise velocity for distinct rotation numbers with $Tr_b = \infty$, i.e. with no-slip boundary condition. By introducing the system rotation, the profiles become asymmetric and by increasing the rotation number, more pronounced asymmetry is observed. The maximum mean velocity moves towards the suction side. As shown by Kristoffersen and Andersson (1993), away from both walls, the profiles are approximately linear with a slope of 2Ω. A key question to be addressed here is whether this geometrical property of mean velocity profiles of the rotating channel is observed when the wall boundary condition is altered from no-slip to slip. Figures 7, 8 and 9 show the profiles of the mean streamwise velocity for various rotation numbers with $Tr_b = 100$, 10 and 1, respectively. The appearance of a linear part of the average velocity profile with a slope of 2Ω is confirmed for slip flows, even at very strong wall slips ($Tr_b = 1$).

The extension of the linear part increases by increasing the rotation number, at low to moderate rotation of the system, similar to that of the rotating channel with no-slip

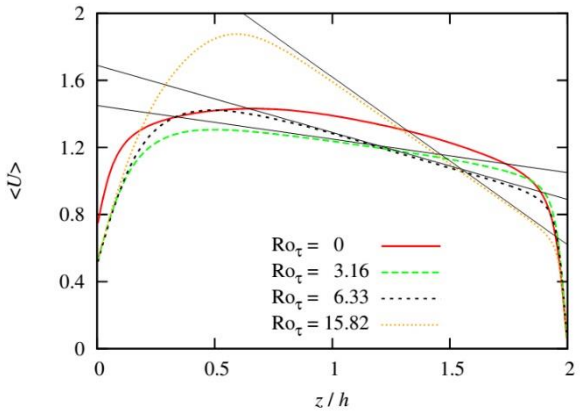

Fig. 8 Mean velocity profiles at different Rotation numbers with $Tr_b = 10$. Thin, black, solid lines represent straight lines with slope 2Ω

condition, as reported by Kristoffersen and Andersson (1993). It indicates that this behavior is mainly controlled

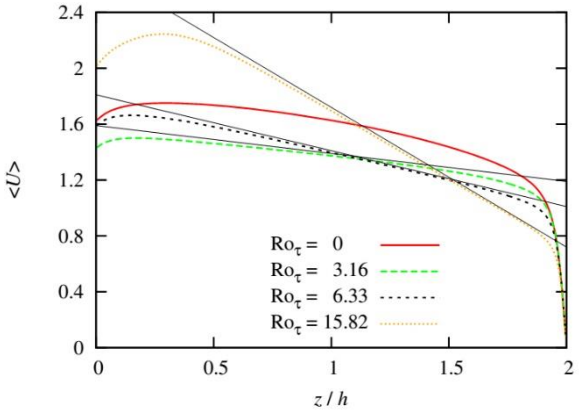

Fig. 9 Mean velocity profiles at different Rotation numbers with $\mathrm{Tr_b} = 1$. Thin, black, solid lines represent straight lines with slope 2Ω

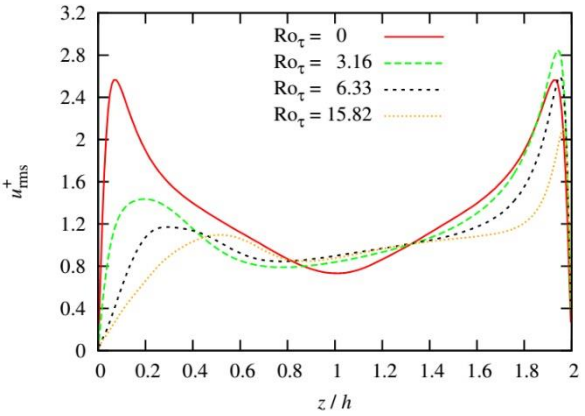

Fig. 10 RMS streamwise velocity fluctuations at different rotation numbers and $\mathrm{Tr_b} = \infty$

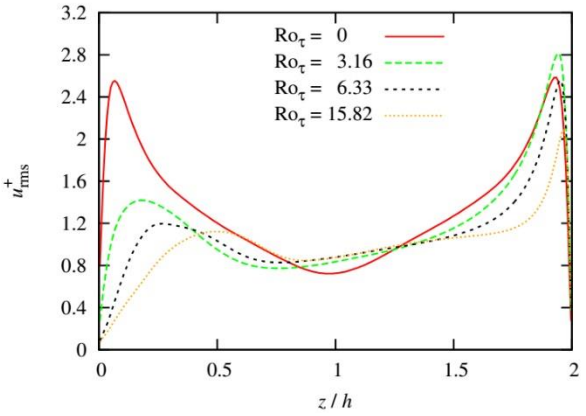

Fig. 11 RMS streamwise velocity fluctuations at different rotation numbers and $\mathrm{Tr_b} = 100$

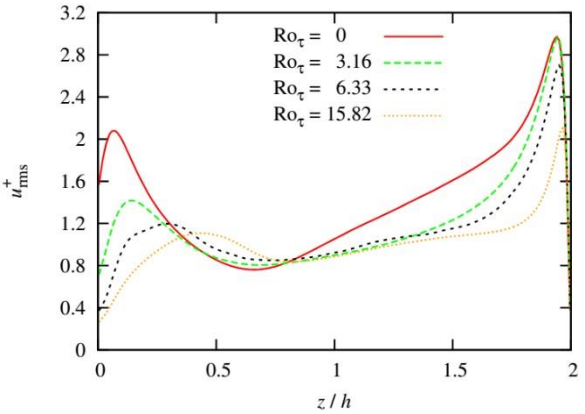

Fig. 12 RMS streamwise velocity fluctuations at different rotation numbers and $\mathrm{Tr_b} = 10$

by the system rotation and the effect of wall boundary condition is modest, if existed at all. The existence of a region with almost a constant slope 2Ω for flow with slip condition means that the absolute mean vorticity $2\Omega - \mathrm{d}\langle U\rangle/\mathrm{d}z$ vanishes in this region. Defining the ratio of the background vorticity 2Ω to the mean shear vorticity $-\mathrm{d}\langle U\rangle/\mathrm{d}z$ as $S = -2\Omega/(\mathrm{d}\langle U\rangle/\mathrm{d}z)$, we have $\mathrm{S} = -1$ in this region. As discussed by Kristoffersen and Andersson (1993), this portion of the mean velocity profile represents a region of neutral stability, i.e. the border between destabilization ($\mathrm{S} > -1$) and stabilization ($\mathrm{S} < -1$). Of course, this conclusion is valid for velocity slip on the suction wall of the channel at the rotation numbers considered here. Whether this holds for slip on the pressure wall or slip on both walls would need further investigations.

An interesting feature of this flow is the amount of slip velocity on the suction wall. For the no-slip condition ($\mathrm{Tr_b} = \infty$), the velocities on the wall vanish. However, by introducing the wall slip condition, a dependency of the wall slippage velocity on both rotation and Trostel numbers can be observed. For relatively large Trostel numbers ($\mathrm{Tr_b} = 100$ and 10), the maximum wall slip velocity is observed for the non-rotating channel and the wall slip velocities for rotating channels coincide.

However, at a small Trostel number ($\mathrm{Tr_b} = 1$), a different trend is seen, i.e. the wall slip velocity first decreases by increasing the rotation number and then it increases, such that the wall slip velocity of $\mathrm{Ro}_\tau = 0$ and $\mathrm{Ro}_\tau = 6.33$ are close to each other.

5.2 RMS Velocity Fluctuations and Reynolds Shear Stress

The turbulence intensities, i.e. RMS velocity fluctuations, in streamwise x, spanwise y and wall-normal z directions are depicted in Figs. 10-21, for various rotation and Trostel numbers. The general trend, with some exceptions, is that the intensities of turbulence have been subdued on the suction wall whereas they have been intensified on the pressure wall, by increasing the rotation number. The exceptions are explained below in details.

In Figs. 10-13, we see that the peaks of u^+_{rms} decrease near the suction wall, where slip exists, while they increase near the pressure wall. Also, the u^+_{rms} profiles lose symmetry by increasing wall slip and/or rotation. By increasing the rotation number at each Trostel number, the peaks move away from the suction wall while they move towards the pressure wall. For $\mathrm{Tr_b} = \infty$ and 100, the peak of u^+_{rms} near the pressure wall first increases and then decreases by increasing the rotation number, whereas, for $\mathrm{Tr_b} = 10$ and 1, the peak only decreases. The trends are qualitatively similar for different Trostel numbers. But, for $\mathrm{Tr_b} = 1$, the behavior is somewhat qualitatively different, as shown in Fig. 14. That is, u^+_{rms} peaks on the wall and

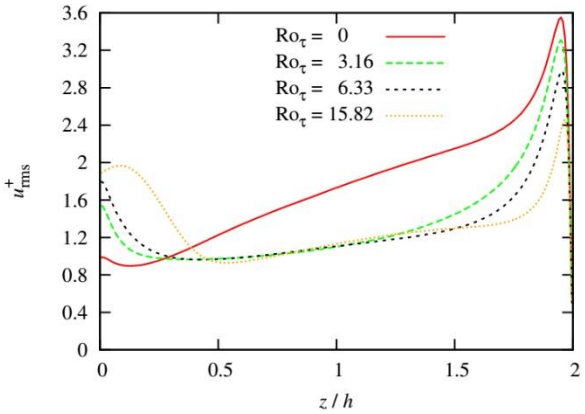

Fig. 13 RMS streamwise velocity fluctuations at different rotation numbers and $\mathrm{Tr_b} = 1$

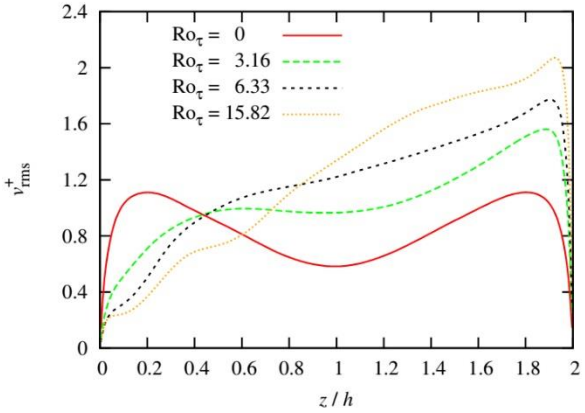

Fig. 14 RMS spanwise velocity fluctuations at different rotation numbers and $\mathrm{Tr_b} = \infty$

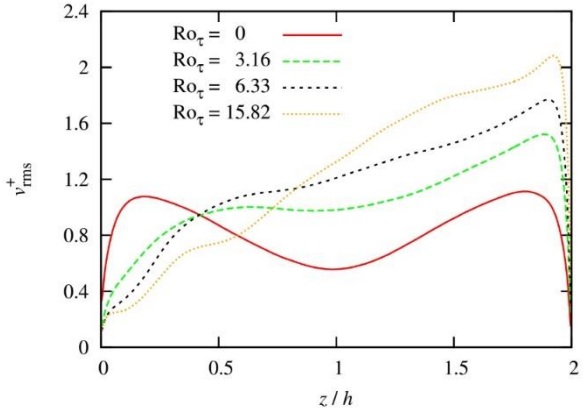

Fig. 15 RMS spanwise velocity fluctuations at different rotation numbers and $\mathrm{Tr_b} = 100$

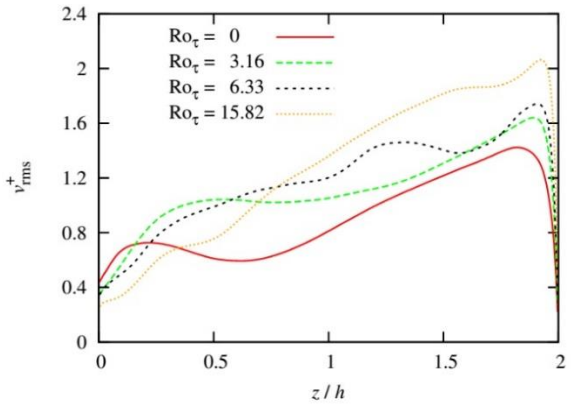

Fig. 16 RMS spanwise velocity fluctuations at different rotation numbers and $\mathrm{Tr_b} = 10$

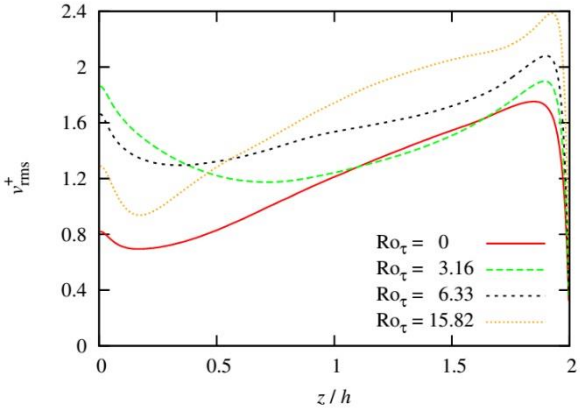

Fig. 17 RMS spanwise velocity fluctuations at different rotation numbers and $\mathrm{Tr_b} = 1$

then has a decreasing trend in the wall vicinity, while, for higher values of Trostel number, the maximum of u^+_{rms} is somewhere away from the wall. Even for $\mathrm{Tr_b} = 1$, u^+_{rms} has a peak away from the wall for relatively strong system rotation $\mathrm{Ro}_\tau = 15.82$.

As shown in Fig. 9, the mean velocity gradient $\partial\langle U\rangle/\partial z$ is significantly decreased near the suction wall for $\mathrm{Tr_b} = 1$. Also, Fig. 25 shows that the Reynolds shear stress is nearly zero at the suction wall for this Trostel number. The combination of these two facts means a tremendous reduction in the turbulence production near the suction wall in this case. However, there exist considerable u^+_{rms} near the suction wall for $\mathrm{Tr_b} = 1$ as shown in Fig. 14, though significantly reduced as compared to the pressure wall. By looking at the evolution equation for the Reynolds stresses, and since the turbulence production is virtually zero at the suction wall for $\mathrm{Tr_b} = 1$, it is conjectured that the turbulence intensity is either transported towards the wall by the Reynolds stress flux term or it comes from other components via the energy redistribution process through the pressure-strain correlation terms. In order to scrutinize this, one has to look at the budget of turbulence intensities or Reynolds stresses, which is not presented in this study.

Figures 14-17 show the behavior of v^+_{rms} for different cases. In general, by increasing the rotation number at each Trostel number, v^+_{rms} decreases near the suction wall while it increases near the pressure wall. Again, the behavior is different for $\mathrm{Tr_b} = 1$, that is, by increasing the rotation number from $\mathrm{Ro}_\tau = 0$ to $\mathrm{Ro}_\tau = 3.16$, v^+_{rms} increases near the suction wall. However, v^+_{rms} decreases by further increasing the rotation number.

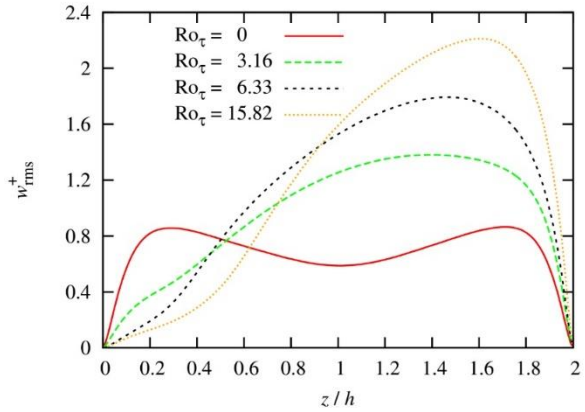

Fig. 18 RMS wall-normal velocity fluctuations at different rotation numbers and $\mathbf{Tr_b = \infty}$

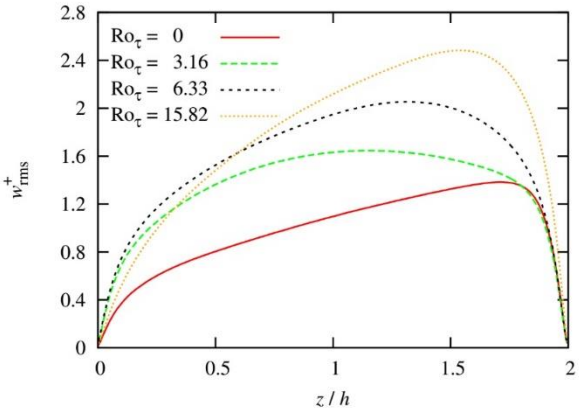

Fig. 21 RMS wall-normal velocity fluctuations at different rotation numbers and $\mathbf{Tr_b = 1}$

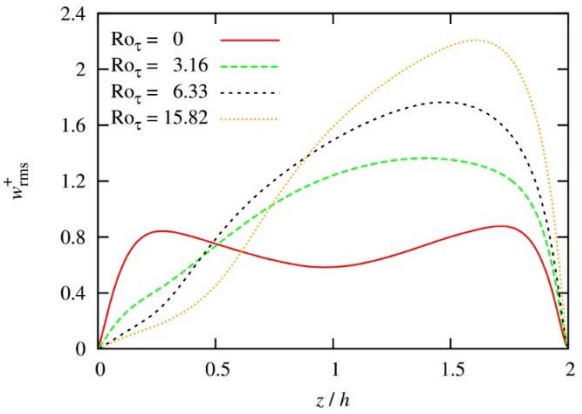

Fig. 19 RMS wall-normal velocity fluctuations at different rotation numbers and $\mathbf{Tr_b = 100}$

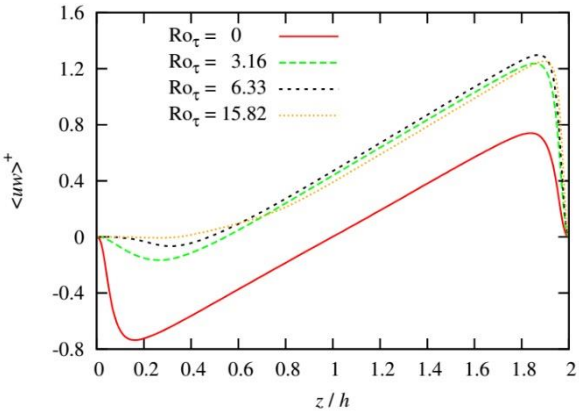

Fig. 22 Reynolds shear stress at different rotation numbers and $\mathbf{Tr_b = \infty}$

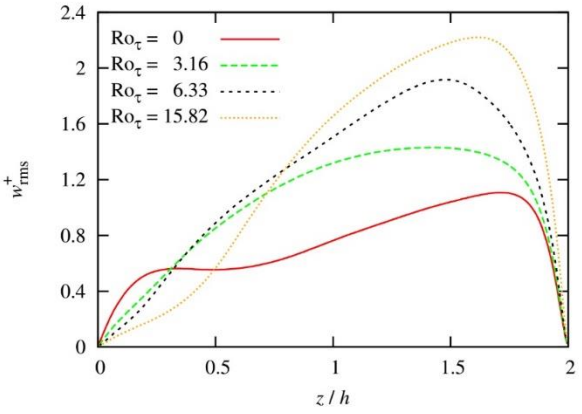

Fig. 20 RMS wall-normal velocity fluctuations at different rotation numbers and $\mathbf{Tr_b = 10}$

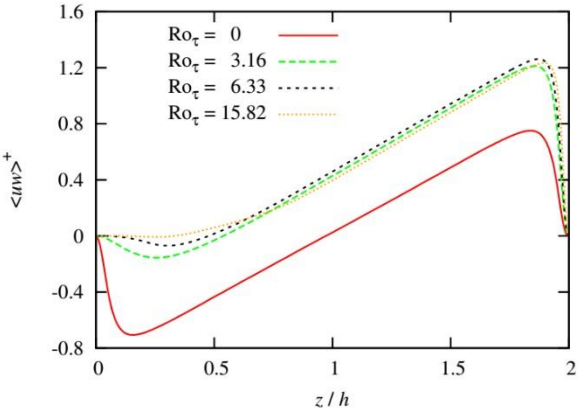

Fig. 23 Reynolds shear stress at different rotation numbers and $\mathbf{Tr_b = 100}$

The RMS wall-normal velocity w^+_{rms} is depicted in figures 18-21 for different cases. We see that the wall-normal fluctuation intensities are subdued near the suction wall while they are pronounced near the pressure wall. This trend is intensified by increasing the rotation number. The exception is $\mathrm{Tr_b} = 1$, for which w^+_{rms} increases near the suction wall.

Figures 22-25 show the Reynolds shear stress $\langle uw \rangle^+$ as a function of z. In general, increasing the rotation reduces the level of $\langle uw \rangle^+$ near the suction side while increases it near the pressure side. Also, the slip at the suction wall has a similar effect. Thus, both effects are synergic in this manner. At $\mathrm{Tr_b} = 1$, the Reynolds shear

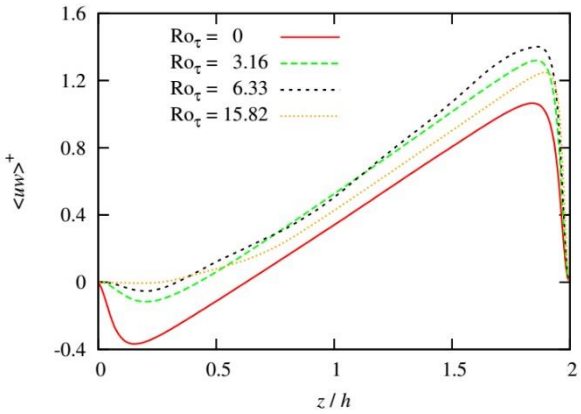

Fig. 24 Reynolds shear stress at different rotation numbers and $\mathbf{Tr_b = 10}$

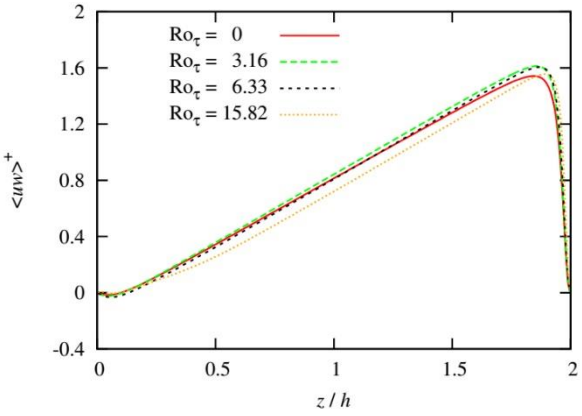

Fig. 25 Reynolds shear stress at different rotation numbers and $\mathbf{Tr_b = 1}$

stress profiles for different rotation numbers are very close to each other. The attenuation of $\langle uw \rangle^+$ near the suction wall results in a weaker production of turbulence in this region.

5.3 Near-Wall Streaks

The near-wall streaks are studied here for the cases of $\mathrm{Ro}_\tau = 0, 6.33$ and $\mathrm{Tr_b} = 10, \infty$. For this purpose, instantaneous streamwise velocity contours at wall distances of $z/h = 0.076$ and $z/h = 1.942$ for these cases are shown in Figs 26 to 32, in which horizontal and vertical axes are respectively x and y. It is observed that both spanwise rotation and wall slip result in a more quiescent flow close to the suction side and a more vigorous flow close the pressure side. By increasing the amount of system rotation rate and the amount of slip, the streaky structures at the shown wall distance gradually disappear, which is an indication of the weakening of the near-wall regeneration mechanism. Thus, the flow at the suction side goes towards laminarization.

To study the streak spacing in the wall proximity region, we look at the two-point streamwise velocity correlation R_{uu} versus the spanwise separation r_y, shown in figure 33 for different cases. Twice the spanwise separation of the first minimum of R_{uu} indicates the

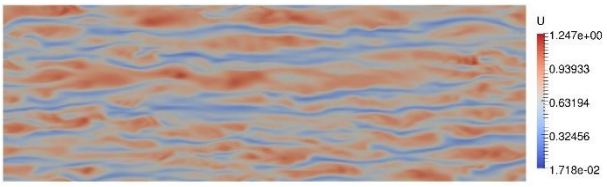

Fig. 26 Instantaneous streamwise velocity contour at $z/h = 0.076$ for $\mathrm{Tr_b} = \infty$ and $\mathrm{Ro}_\tau = 0$

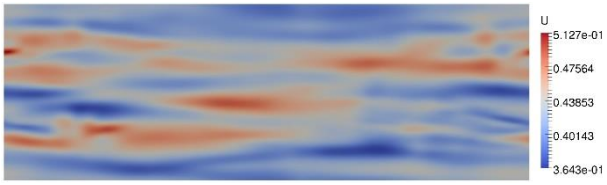

Fig. 27 Instantaneous streamwise velocity contour at $z/h = 0.076$ for $\mathrm{Tr_b} = \infty$ and $\mathrm{Ro}_\tau = 6.33$

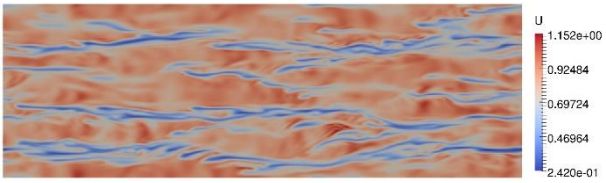

Fig. 28 Instantaneous streamwise velocity contour at $z/h = 1.942$ for $\mathrm{Tr_b} = \infty$ and $\mathrm{Ro}_\tau = 6.33$

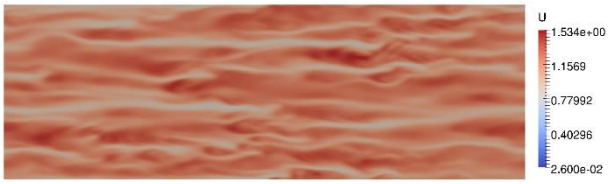

Fig. 29 Instantaneous streamwise velocity contour at $z/h = 0.076$ for $\mathrm{Tr_b} = 10$ and $\mathrm{Ro}_\tau = 0$

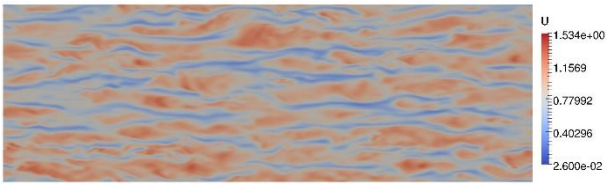

Fig. 30 Instantaneous streamwise velocity contour at $z/h = 1.942$ for $\mathrm{Tr_b} = 10$ and $\mathrm{Ro}_\tau = 0$

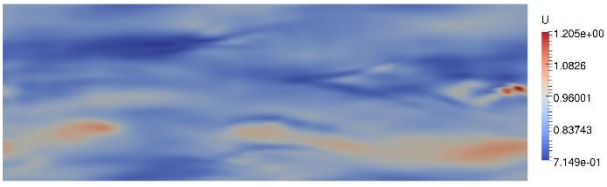

Fig. 31 Instantaneous streamwise velocity contour at $z/h = 0.076$ for $\mathrm{Tr_b} = 10$ and $\mathrm{Ro}_\tau = 6.33$

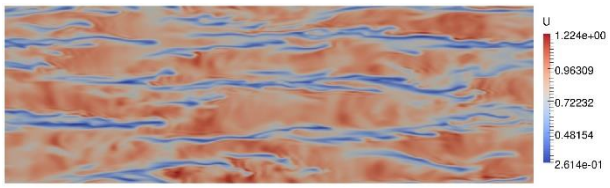

Fig. 32 Instantaneous streamwise velocity contour at $z/h = 1.942$ for $\mathrm{Tr_b} = 10$ and $\mathrm{Ro}_\tau = 6.33$

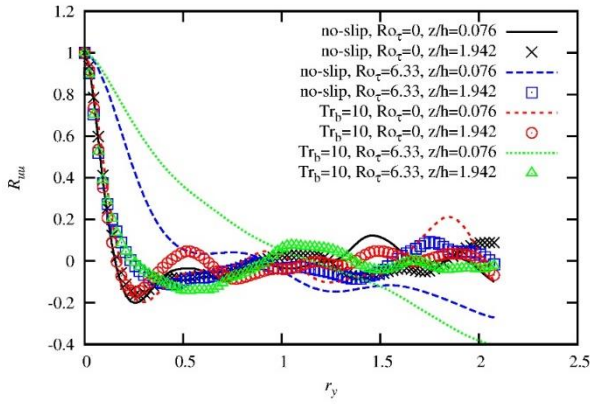

Fig. 33 Two-point streamwise velocity correlation in spanwise direction for different cases

Fig. 34 Instantaneous streamwise vorticity contour ($\omega_x h/U_{\mathrm{b,nos}} = 2$) in the xz-plane for $\mathrm{Tr_b} = \infty$ and $\mathrm{Ro}_\tau = 0$

average spanwise spacing between near-wall streaks. We observe that for $\mathrm{Ro}_\tau = 6.33$, the streaky structures near the suction wall are not well recognized and this is indicated by the correlation profiles of these cases. This can be attributed to the reduction in the apparent friction Reynolds number which in turn leads to an increase in the streak spacing relative to the channel width. This effect is more severe for the case with wall slip as compared to the no-slip case. The mean streak spacing near the pressure side dramatically increases by increasing the rotation number. However, the effect of slip over the suction wall on the streak spacing of the pressure wall is modest.

5.4 Instantaneous Streamwise Vorticity

Streamwise vorticity is well-known to be important in the near-wall regeneration mechanism and thus, in the near-wall production of turbulence which is vital for turbulence to be sustained. Thus, the streamwise vorticity contour ($\omega_x h/U_{\mathrm{b,nos}} = 2$) are plotted in Figs 34 to 37 for different cases. For the no-slip case without system rotation, a symmetric pattern is observed and the intensity of streamwise vorticity on both walls is similar. System rotation and suction wall slip result in an asymmetric pattern, however, the effect of rotation is much more pronounced.

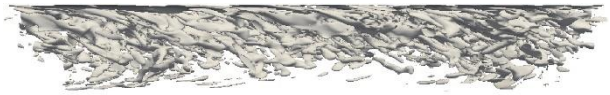

Fig. 35 Instantaneous streamwise vorticity contour ($\omega_x h/U_{\mathrm{b,nos}} = 2$) in the xz-plane for $\mathrm{Tr_b} = \infty$ and $\mathrm{Ro}_\tau = 6.33$

Fig. 36 Instantaneous streamwise vorticity contour ($\omega_x h/U_{\mathrm{b,nos}} = 2$) in the xz-plane for $\mathrm{Tr_b} = 10$ and $\mathrm{Ro}_\tau = 0$

Fig. 37 Instantaneous streamwise vorticity contour ($\omega_x h/U_{\mathrm{b,nos}} = 2$) in the xz-plane for $\mathrm{Tr_b} = 10$ and $\mathrm{Ro}_\tau = 6.33$

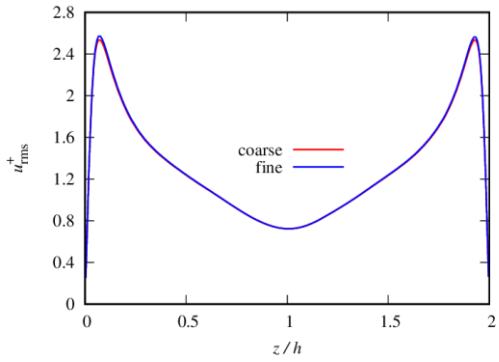

Fig. 38 RMS streamwise velocity fluctuations for $\mathrm{Tr_b} = \infty$ and $\mathrm{Ro}_\tau = 0$ obtained from coarse and fine simulations

6. A NOTE ON COMPUTATIONAL COSTS AND GRID INDEPENDENCE

Each run was performed on a single core of a Core i7-4790K CPU with a CPU-clock of 4.00 GHz made by Intel. The system had 16 GB of RAM. On the above platform, we spent about 5 CPU-seconds per time step for each run. Each simulation was running with 100000 time steps, of which, the first 33000 time steps were used for flow development and the next 67000 time steps were used for the collection of flow statistics.

In order to make sure that the results are grid-independent, we have conducted a finer simulation using $(N_x, N_y, N_z) = (244, 200, 148)$ for the case with $\mathrm{Re}_\tau = 194$, $\mathrm{Tr_b} = \infty$ and $\mathrm{Ro}_\tau = 0$. For the sake of brevity, only u^+_{rms} is shown in Fig. 38 and compared with that of the coarser simulation. The agreement is quite good. Small discrepancies are observed at the near-wall peaks.

7. CONCLUSION

Direct numerical simulation of turbulent channel flow rotating about its spanwise axis with one hydrophobic wall is reported. This flow has two sources of asymmetry about the channel centerline; the system rotation and the slip condition on the suction wall. It is found that both effects result in the asymmetry of mean quantities about the channel centerline. Similar to no-slip spanwise rotating channel, there exists a linear portion of the mean velocity profile whose width increases by increasing the rotation number. The exception is for small Trostel number ($Tr_b = 1$), i.e. turbulence intensities increase close the suction side by increasing the rotation number. Reynolds shear stress reduces close the suction side whereas it increases near the pressure side. Both system rotation and suction wall slip result in a more quiescent flow close to the suction wall and a more vigorous flow close to the pressure wall. The streak spacing near the pressure side increase dramatically by system rotation, whereas the effect of wall slip is modest. Both rotation and slip affect the streaky structures to gradually disappear near the suction side. The streamwise vorticity which has a pivotal role in the near-wall regeneration mechanism and thus in the sustainment of turbulence is weakened near the suction side while it is intensified near the pressure side. The influence of system rotation is much more pronounced. This is in line with the laminarization of the flow near the suction side. The findings of this research would be of interest from a fundamental view as well as for applications involving turbulent drag reduction in rotating systems. As an outlook for future research, the influence of the wall slip condition on the pressure wall alone and simultaneously on both suction and pressure walls could be investigated. Moreover, the simultaneous effects of system rotation and wall slip in other flow configurations, e.g. a flat-plate boundary layer, could be studied. Moreover, we considered a constant slip parameter in the present work. The effect of variable slip parameter and the variation of slip parameter in the streamwise and spanwise directions could be studied as well.

CONFLICT OF INTEREST

The authors declare that they have no known competing financial interests or personal relationships that could have appeared to influence the work reported in this paper.

AUTHORS CONTRIBUTION

A. Moosaie: Conceptualization, Investigation, Methodology, Project administration, Software, Resources, Supervision, Validation, Writing – original draft, Writing – review & editing, **Zh. Najafi-Kashkooli**: Data curation, Formal analysis, Investigation, Visualization, Writing – original draft, **H. I. Andersson**: Project administration, Supervision, Writing – review & editing.

REFERENCES

Atefi, G. (1991). Quer angeströmter drehender Zylinder bei kleinen Reynoldszahlen und bei Schlupf. *Archive of Applied Mechanics*, *61*(7), 488-502. https://doi.org/10.1007/BF00705241

Bech, K. H., & Andersson, H. I. (1997). Turbulent plane Couette flow subject to strong system rotation. *Journal of Fluid Mechanics*, *347*, 289-314. https://doi.org/10.1017/S002211209700670X

Blasius, H. (1908). Grenzschichten in Flüssigkeiten mit kleiner Reibung. *Zeitschrift für Mathematik und Physik*, 56, 1-37.

Busse, A., & Sandham, N. D. (2012). Influence of an anisotropic slip-length boundary condition on turbulent channel flow. *Physics of Fluids*, *24*(5), 055111. https://doi.org/10.1063/1.4717732

Choi, C., Westin, K. J. A., & Breuer, K. S. (2003). Apparent slip flows in hydrophilic and hydrophobic microchannels. *Physics of Fluids*, *15*(10), 2897-2902. https://doi.org/10.1063/1.1605425

Chorin, A. J. (1968). Numerical solution of the Navier-Stokes equations. *Mathematics of Computation*, *22*(104), 745-762. https://doi.org/10.1090/S0025-5718-1968-0242392-2

Grundestam, O., Wallin, S., & Johansson, A. V. (2008). Direct numerical simulations of rotating turbulent channel flow. *Journal of Fluid Mechanics*, *598*, 177-199. https://doi.org/10.1017/S0022112008000046

Jagadeesan, K., Narasimhamurthy, V. D., & Andersson, H. I. (2022). The structure of turbulence in rotating rough-channel flows. *International Journal of Heat and Fluid Flow*, *95*, 108956. https://doi.org/10.1016/j.ijheatfluidflow.2022.108956

Johnston, J. P., Halleen, R. M., & Lezius, D. K. (1972). Effects of spanwise rotation on the structure of two-dimensional fully developed turbulent channel flow. *Journal of Fluid Mechanics*, *56*, 533-557. https://doi.org/10.1017/S0022112072000257

Kristoffersen, R., & Andersson, H. I. (1993). Direct simulations of low-Reynolds-number turbulent flow in a rotating channel. *Journal of Fluid Mechanics*, *256*, 163-197. https://doi.org/10.1017/S0022112093002834

Launder, B. E., & Tselepidakis, D. P. (1994). Application of a new second-moment closure to turbulent channel flow rotating in orthogonal mode. *International Journal of Heat and Fluid Flow*, *15*(1), 2-10. https://doi.org/10.1016/0142-727X(94)90028-0

Launder, B. E., Tselepidakis, D. P., & Younis, B. A. (1987). A second-moment closure study of rotating channel flow. *Journal of Fluid Mechanics*, *183*, 63-75. https://doi.org/10.1017/S0022112087002556

Maciel, Y., Picard, D., Yan, G., & Dumas, G. (2003, June 23-26). *Fully developed turbulent channel flow*

subject to system rotation. 33rd AIAA Fluid Dynamics Conference. Orlando, FL. https://doi.org/10.2514/6.2003-4153

Manhart, M. (2004). A zonal grid algorithm for DNS of turbulent boundary layers. *Computers & Fluids*, *33*(3), 435-461. https://doi.org/10.1016/j.compfluid.2003.08.001

Martell, M. B., Perot, J. B., & Rothstein, J. P. (2009). Direct numerical simulations of turbulent flows over superhydrophobic surfaces. *Journal of Fluid Mechanics*, *620*, 31-41. https://doi.org/10.1017/S0022112008005010

Martell, M. B., Rothstein, J. P., & Perot, J. B. (2010). An analysis of superhydrophobic turbulent drag reduction mechanisms using direct numerical simulation. *Physics of Fluids*, *22*(6), 065102. https://doi.org/10.1063/1.3428758

Martin, M. J., & Boyd, I. D. (2006). Momentum and heat transfer in a laminar boundary layer with slip flow. *AIAA Journal of Thermophysics and Heat Transfer*, *20*(4), 710-719. https://doi.org/10.2514/1.18039

Martin, M. J., & Boyd, I. D. (2010). Falkner-Skan flow over a wedge with slip boundary conditions. *AIAA Journal of Thermophysics and Heat Transfer*, *24*(2), 263-270. https://doi.org/10.2514/1.41998

Min, T., & Kim, J. (2004). Effects of hydrophobic surface on skin-friction drag. *Physics of Fluids*, *16*(1), 55-58. https://doi.org/10.1063/1.1624832

Min, T., & Kim, J. (2005). Effects of hydrophobic surface on stability and transition. *Physics of Fluids*, *17*(10), 108106. https://doi.org/10.1063/1.2073255

Moosaie, A. (2016). DNS of turbulent drag reduction in a pressure-driven rod-roughened channel flow by microfiber additives. *Journal of Non-Newtonian Fluid Mechanics*, *232*, 1-10. https://doi.org/10.1016/j.jnnfm.2016.03.005

Moosaie, A. (2022). Correction to: G. Atefi, Quer angeströmter drehender Zylinder bei kleinen Reynoldszahlen und bei Schlupf. *Archive of Applied Mechanics*, *92*(10), 3065-3066. https://doi.org/10.1007/s00419-022-02233-y

Moosaie, A. (2024). Stokes-type conjugate heat transfer and thermoelasticity analysis of a hollow spherical particle in a slip flow. *International Communications in Heat and Mass Transfer*, *159*, 108110. https://doi.org/10.1016/j.icheatmasstransfer.2024.108110

Moosaie, A. (2025). Approximate analytical and numerical investigation of Oseen-type forced convection around a sphere in a low Reynolds number slip flow. *International Journal of Thermal Sciences*, *210*, 109556. https://doi.org/10.1016/j.ijthermalsci.2024.109556

Moosaie, A., & Manhart, M. (2011). An algebraic closure for the DNS of fiber-induced turbulent drag reduction in a channel flow. *Journal of Non-Newtonian Fluid Mechanics*, *166*(12), 1190-1197. https://doi.org/10.1016/j.jnnfm.2011.05.002

Moosaie A., & Sharifian A. (2024). Numerical simulation of steady incompressible slip flow around a circular cylinder at low Reynolds numbers, *Acta Mechanica*, *235*, 6791-6811, 2024. https://doi.org/10.1007/s00707-024-04071-1

Moosaie, A., & Manhart, M. (2013). Direct Monte-Carlo simulation of turbulent drag reduction by rigid fibers in a channel flow. *Acta Mechanica*, *224*(10), 2385-2413. https://doi.org/10.1007/s00707-013-0916-x

Moosaie, A., & Manhart, M. (2015). On the structure of vorticity and near-wall partial enstrophy in fibrous drag-reduced turbulent channel flow. *Journal of Non-Newtonian Fluid Mechanics*, *223*, 249-256. https://doi.org/10.1016/j.jnnfm.2015.06.003

Moosaie, A., & Manhart, M. (2016). On the pressure-strain correlation in fibrous drag-reduced turbulent channel flow. *Physics of Fluids*, *28*(2), 025101. https://doi.org/10.1063/1.4940772

Moosaie, A., & Panahi-Kalus, H. (2021). Direct numerical simulation of turbulent heat transfer with slip and temperature jump. *AIAA Journal of Thermophysics and Heat Transfer*, *35*(3), 580-588. https://doi.org/10.2514/1.T6136

Moosaie, A., Shekouhi, N., Nouri, N. M., & Manhart, M. (2015). An algebraic closure model for the DNS of turbulent drag reduction by Brownian microfiber additives in a channel flow. *Journal of Non-Newtonian Fluid Mechanics*, *226*, 60-66. https://doi.org/10.1016/j.jnnfm.2015.10.004

Nakabayashi, K., & Kitoh, O. (1996). Low Reynolds number fully developed two-dimensional turbulent channel flow with system rotation. *Journal of Fluid Mechanics*, *315*, 1-29. https://doi.org/10.1017/S0022112096002282

Nakabayashi, K., & Kitoh, O. (2005). Turbulence characteristics of two-dimensional channel flow with system rotation. *Journal of Fluid Mechanics*, *528*, 355-377. https://doi.org/10.1017/S0022112004003397

Narasimhamurthy, V. D., & Andersson, H. I. (2015). Turbulence statistics in a rotating ribbed channel. *International Journal of Heat and Fluid Flow*, *51*, 29-41. https://doi.org/10.1016/j.ijheatfluidflow.2014.10.010

Ou, J., Perot, J. B., & Rothstein, J. (2004). Laminar drag reduction in microchannels using superhydrophobic surfaces. *Physics of Fluids*, *16*(12), 4635–4643. https://doi.org/10.1063/1.1812011

Park, H., Park, H., & Kim, J. (2013). A numerical study of the effects of superhydrophobic surface on skin-friction drag in turbulent channel flow. *Physics of Fluids*, *25*(11), 110815. https://doi.org/10.1063/1.4828785

Schumann, U. (1975). Subgrid scale model for finite difference simulations of turbulent flows in plane channels and annuli. *Journal of Computational*

Physics, *18*(4), 376-404. https://doi.org/10.1016/0021-9991(75)90093-5

Speziale, C. G., & Thangam, S. (1983). Numerical study of secondary flows and roll-cell instabilities in rotating channel flow. *Journal of Fluid Mechanics*, *130*, 377-395. https://doi.org/10.1017/S0022112083001240

Stone, H. L. (1968). Iterative solution of implicit approximations of multidimensional partial differential equations. *SIAM Journal on Numerical Analysis*, *5*(3), 530-538. https://doi.org/10.1137/0705044

Temam, R. (1969). Sur l'approximation de la solution des équations de Navier-Stokes par la méthode des pas fractionnaires (II). *Archive for Rational Mechanics and Analysis*, *33*, 377-385. https://doi.org/10.1007/BF00247688

Tretheway, D. C., & Meinhart, C. D. (2002). Apparent fluid slip at hydrophobic microchannel walls. *Physics of Fluids*, *14*(3), L9-L12. https://doi.org/10.1063/1.1432696

Visscher, J., & Andersson, H. I. (2011). Particle image velocimetry measurements of massively separated turbulent flows with rotation. *Physics of Fluids*, *23*(7), 075108. https://doi.org/10.1063/1.3611017

Visscher, J., Andersson, H. I., Barri, M., Didelle, H., Viboud, S., Sous, D., & Sommeria, J. (2011). A new set-up for PIV measurements in rotating turbulent duct flows. *Flow Measurement and Instrumentation*, *22*(1), 71-80. https://doi.org/10.1016/j.flowmeasinst.2010.12.002

Wang, W., Niu, X., Fan, K., & Wang, Q. (2011). Stokes' second problem with velocity slip boundary condition. *Key Engineering Materials*, *483*, 287-292. https://doi.org/10.4028/www.scientific.net/KEM.483.287

Watanabe, K., Udagawa Y., & Udagawa, H. (1999). Drag reduction of Newtonian fluid in a circular pipe with a highly water-repellent wall. *Journal of Fluid Mechanics*, *381*, 225-238. https://doi.org/10.1017/S0022112098003743

Williamson, J. H. (1980). Low-storage Runge-Kutta schemes. *Journal of Computational Physics*, *35*(1), 48-56. https://doi.org/10.1016/0021-9991(80)90033-9

Youngblood, J. P., Andruzzi, L., Ober, C. K., Hexemer, A., Kramer, E. J., Callow, J. A., Finlay, J. A., & Callow, M. E. (2003). Coating based on side-chain ether-linked poly (ethylene glycol) and fluorocarbon polymers for the control of marine biofouling. *Biofouling*, *19*(2), 91-98. https://doi.org/10.1080/0892701021000057886.